nanomaterials

MDPI

Article

Controlled Hydrothermal Growth and Li^+ Storage Performance of 1D VO_x Nanobelts with Variable Vanadium Valence

Yuhan Jiang [1], Xiaowei Zhou [1,*], Xu Chen [1], Jia Wen [1], Linlin Guan [1], Mingxia Shi [1], Yang Ren [1] and Zhu Liu [1,2,*]

[1] Department of Physics, School of Physics and Astronomy, Yunnan University, Kunming 650504, China; jiangyuhan1994@mail.ynu.edu.cn (Y.J.); chenxu@ynu.edu.cn (X.C.); wen__jia@163.com (J.W.); ninin0621@163.com (L.G.); smx303@126.com (M.S.); reny@lzu.edu.cn (Y.R.)

[2] Yunnan Key Laboratory of Micro/Nano-Materials and Technology, Yunnan University, Kunming 650504, China

* Correspondence: zhouxiaowei@ynu.edu.cn (X.Z.); zhuliu@ynu.edu.cn (Z.L.)

Received: 29 March 2019; Accepted: 15 April 2019; Published: 17 April 2019

Abstract: One-dimensional (1D) vanadium oxide nanobelts (VO_x NBs) with variable V valence, which include $V_3O_7{\cdot}H_2O$ NBs, VO_2 (B) NBs and V_2O_5 NBs, were prepared by a simple hydrothermal treatment under a controllable reductive environment and a following calcination process. Electrochemical measurements showed that all these VO_x NBs can be adopted as promising cathode active materials for lithium ion batteries (LIBs). The Li^+ storage mechanism, charge transfer property at the solid/electrolyte interface and Li^+ diffusion characteristics for these as-synthesized 1D VO_x NBs were systematically analyzed and compared with each other. The results indicated that V_2O_5 NBs could deliver a relatively higher specific discharge capacity (213.3 mAh/g after 50 cycles at 100 mA/g) and median discharge voltage (~2.68–2.71 V vs. Li/Li^+) during their working potential range when compared to other VO_x NBs. This is mainly due to the high V valence state and good crystallinity of V_2O_5 NBs, which are beneficial to the large Li^+ insertion capacity and long-term cyclic stability. In addition, the as-prepared VO_2 (B) NBs had only one predominant discharge plateau at the working potential window so that it can easily output a stable voltage and power in practical LIB applications. This work can provide useful references for the selection and easy synthesis of nanoscaled 1D vanadium-based cathode materials.

Keywords: vanadium oxide nanobelts; controlled hydrothermal synthesis; variable vanadium valence; cathode materials; Li^+ storage performance

1. Introduction

The efficient storage and release of electric energy is an important topic in the field of energy storage research. At present, two kinds of energy storing devices, that is, lithium ion batteries (LIBs) and supercapacitors (SCs), have received great attention because of their respective features in high energy density and power density. As one of the typical energy storage units, LIBs are widely applied in various consumer electronics and electric tools since they have the advantages of large energy density, low self-discharge rate, no memory effect, etc. Electrode materials are directly responsible for the electrochemical performance of LIBs. It is crucial for the development of cathode materials with large capacities, high working voltage and high rate capability. Traditional cathode materials for LIBs, such as $LiCoO_2$, $LiMn_2O_4$, $LiNi_xCo_yMn_zO_2$ and $LiFePO_4$, which only possess a specific capacity of ~120–180 mAh/g, could not meet the requirement of high-energy density for next generation LIBs [1]. Thus, it is necessary to explore new-type cathodes with large capacity. Among the diverse transition

metal oxides, vanadium oxide (VO_x) could act as a kind of promising cathode candidate with relatively high operating voltage and capacity during the Li^+ intercalation/de-intercalation process, which was noted very early by researchers and battery manufacturers [2,3].

There are a wide variety of configurations for VO_x including V_2O_5, V_3O_7, VO_2, V_6O_{13}, etc. To improve the electrochemical performance of the VO_x matrix (mainly the conductivity and structural stability upon the repeated charge/discharge), the commonly adopted methods are the design of nanostructure and further modifications, like doping, as well as combination with conductive frameworks [3–5]. The reported nanostructures involve 0-Dimensional (0D) (nanosphere and nanoparticle), 1D (nanobelt, nanofiber, nanorod and nanowire), 2D (nano-film, nanoplate and nanosheet) and 3D hierarchical (nanoflower, nanourchin and mesoporous structure) VO_x, which were produced through various methods, such as template synthesis, self-assembly, hydrothermal process, sol-gel, spray pyrolysis, electro-spinning and chemical vapor deposition (CVD) [4–9]. The electrochemical Li^+ storage performance of these VO_x nanostructures is significantly superior to those of their bulk counterparts and commercial cathodes. During a variety of VO_x nanostructures, one-dimensional (1D) VO_x has the advantages of convenient synthesis, structural simplicity and easy to scale-up production, which makes VO_x prospective as alternative cathode materials for LIBs. In recent years, the solvothermal method was mainly applied to prepare 1D V_3O_7, VO_2 and V_2O_5 nanobelts, whose specific capacity and Li^+ storage properties were investigated under different working voltage windows [10–15]. However, it is rarely reported that a series of 1D nanostructured VO_x, which possess variable components and crystal structures, were acquired in a similar synthetic environment just by altering reaction reagents and combining them with a simple post-treatment.

During our study, we propose an easy route to prepare 1D VO_x nanostructures with different crystalline textures and vanadium valence states based on hydrothermal treatment. For one thing, 1D $V_3O_7{\cdot}H_2O$ and VO_2 (B) nanobelts (NBs) with relatively low V valence were obtained through the previous solation of V_2O_5 powder and introduction of reducing ingredients (ethanol and CNTs) under hydrothermal condition. For another, V_2O_5 NBs with high V valence were further achieved by simple post-sintering to VO_x NBs in air under the circumstance of maintaining the 1D nanobelt shape. The microscopic morphologies, crystal lattices and V-O bonding of these 1D VO_x NBs were characterized and analyzed. When these VO_x NBs were used as active cathodes for LIBs, their Li^+ storage properties were evaluated and compared systematically. According to this research, we get a simple method to obtain 1D VO_x NBs with variable V valence on a large scale. In addition, the micro-architecture and electrochemical Li^+ insertion/extraction performance of these VO_x NBs were discussed and perceived.

2. Experimental Section

2.1. Sample Preparations

All reaction reagents were analytically pure grade and used as received.

Firstly, 1.82 g of V_2O_5 (Shanghai Kefeng industrial Co., Ltd., Shanghai, China) powder (referring to ESI, Figure S1) was dispersed into 75 ml of de-ionized water (self-produced by EPED-10TH apparatus from Nanjing Yipu Yida technology development Co. Ltd., Nanjing, China) with strong magnetic stirring, which formed a yellow suspension. Then, 5 ml of H_2O_2 (30%, mass concentration, Tianjin Fengchuan chemical reagent co. Ltd., Tianjin, China) was poured to the above V_2O_5 suspension under continuous agitation for 5 hours, generating translucent and orange V_2O_5 sol. After that, ~80 ml of V_2O_5 sol was further mixed with 0.2 ml of absolute ethanol (Tianjin Fengchuan) and transferred into a 100 ml of Teflon-lined hydrothermal autoclave (100 ml, Shanghai Lingtuo instrument and equipment Co., Ltd., Shanghai, China). The stainless steel reactor was sealed, kept at 180 °C for 2 days in an electric heating oven and cooled to room temperature naturally. The resultant black precipitate was rinsed, filtrated and dried at 80 °C. The sample obtained was labeled as $V_3O_7{\cdot}H_2O$ nanobelts (NBs).

In order to study the effect of ethanol content on the final product, 2 ml of absolute ethanol was added to previously described V_2O_5 sol (80ml) and followed by hydrothermal treatment with identical operating procedures. The product was denoted as $V_3O_7{\cdot}H_2O/VO_2$ (B)* NBs.

For further comparison, 2 ml of ethanol and 0.2 g of multi-walled carbon nanotubes (MWCNTs, Shenzhen Nanotech Port Co., Ltd., Shenzhen, China) were simultaneously introduced into the above mentioned V_2O_5 (80 ml) sol under ultrasonic oscillation, forming black turbid liquid that was also subjected to the same hydrothermal process. The MWCNTs used here were previously treated with the mixed concentrated acid (H_2SO_4:HNO_3 = 3:1, volume ratio, Chengdu Kelong Chemical Reagent Factory, Chengdu, China) in order to create the surface functional groups and enhance their dispersibility in water. The collected powder has a dark black-blue color, which is labeled as VO_2 (B) NBs/MWCNTs. The filling degree for autoclave during all hydrothermal reactions was controlled at 80%.

V_2O_5 NBs were prepared by directly sintering the previously acquired $V_3O_7{\cdot}H_2O$ NBs in a tube furnace (OTF-1200X, Hefei Kejing-MTI technology Co., Ltd., Hefei, China) at 400 °C for 3 hours under air condition with the ramping rate of 5 °C/min.

2.2. Characterizations

A scanning electron microscope (SEM, QUANTA 200, FEI Company, Hillsboro, OR, USA) was employed to observe the surface morphologies of the as-prepared samples. The crystal structures of the products were determined by X-Ray Diffractometer (XRD, TTRIII-18KW, Rigaku, Tokyo, Japan) at the 2θ angle range of 10–90° (recording interval, 0.02°) with Cu Kα radiation (λ = 1.5406 Å). Transmission electron microscope (TEM, JEM-2100, JEOL, Akishima, Tokyo, Japan) equipped with the module for Selected area electron diffraction (SAED) was applied to examine the microstructures of samples. Material composition and atomic bonding for the products obtained were analyzed through Fourier transform infrared (FTIR) spectroscope with a Bruker-TENSOR27 (Bruker Optics, Karlsruhe, Germany) spectrometer at wave number region of 400–4000 cm^{-1} using KBr pellets.

2.3. Electrochemical Tests

The cathode slurry was composed of active material ($V_3O_7{\cdot}H_2O$ NBs, $V_3O_7{\cdot}H_2O/VO_2$ (B)* NBs, VO_2 (B) NBs/MWCNTs or V_2O_5 NBs), conductive acetylene black (Shenzhen Kejing Zhida-MTI technology Co., Ltd., Shenzhen, China) and polyvinylidene fluoride (PVDF, Shenzhen Kejing), with a mass ratio of 7:2:1, using N-methyl-2-pyrrolidone (NMP, Shenzhen Kejing) as an organic solvent. The slurry was uniformly coated onto the Al foil (Shenzhen Kejing) by a doctor blade and dried at 120 °C over 8 h in a vacuum to wipe off the NMP completely. Then, the formative cathode plate was cut into circular discs of 12 mm in diameter for electrochemical performance evaluations and the average active material loaded for all electrodes was ~1.4 mg/cm^2. Coin cells (CR-2025, Shenzhen Kejing) were assembled by using the cathode disc as a working electrode, a porous polyolefin tri-layer membrane (Celgard 2325, Shenzhen Kejing) as a separator and Li metal as reference/counter electrode. A 1 M $LiFP_6$ dissolved in ethylene carbonate/dimethyl carbonate/ethyl methylcarbonate (EC/DMC/EMC, 1/1/1, volume ratio, Shenzhen Kejing) was adopted as an electrolyte. The battery assembly was performed in a glove box with inert Ar atmosphere where both H_2O and O_2 gas were below 1 ppm.

Cyclic voltammograms (CV) were recorded by an electrochemical workstation (CHI660, Shanghai Chenhua metrologic instruments Co., Ltd., Shanghai, China) at a scanning speed of 0.2 mV s^{-1} within the voltage region of 1.5–4 V or 2–4 V. Galvanostatic charge/discharge (GCD) tests were conducted using LAND (CT2001A, Wuhan Landian electronic Co., Ltd., Wuhan, China) cell-testing system between 1.5–4 V or 2–4 V under specific current densities. Electrochemical impedance spectroscopy (EIS) was also collected by CHI660 electrochemical workstation at the frequency region from 100 k to 0.01 Hz under the state of charge (SOC) of ~3 V with an alternating current (AC) signal of 5 mV. Nyquist plots were fitted by Z-view software.

3. Result and Discussion

Figure 1 shows the synthetic process for $V_3O_7{\cdot}H_2O$ NBs, VO_2 (B) NBs/MWCNTs and V_2O_5 NBs, whose microscopic molecular crystal structures are illustrated in the insets. The $V_3O_7{\cdot}H_2O$ NBs with V^{4+} and V^{5+} coexisting was prepared through hydrothermal reaction using V_2O_5 sol as a precursor and ethanol as a weak reducing agent. When increasing the amount of ethanol and simultaneously introducing MWCNTs as an auxiliary reducing ingredient, VO_2 (B) NBs with predominant V^{4+} were obtained at the same condition. After direct sintering in the air at 400 °C for 3 h, $V_3O_7{\cdot}H_2O$ NBs were transformed into V_2O_5 NBs with complete V^{5+}.

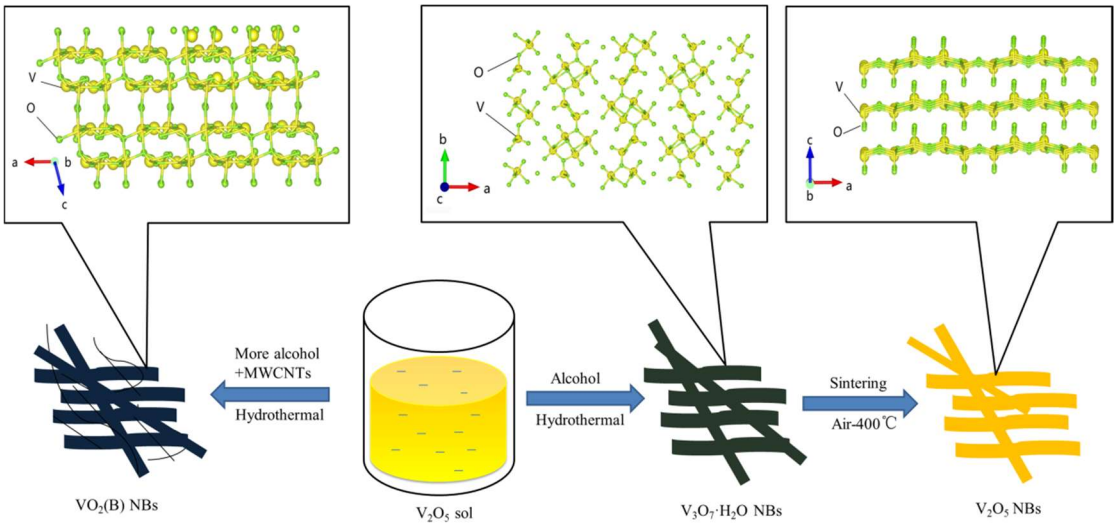

Figure 1. Schematic diagram for preparation of $V_3O_7{\cdot}H_2O$ NBs, VO_2 (B) NBs/MWCNTs and V_2O_5 NBs as well as their corresponding molecular crystal structures.

XRD patterns of all nanostructured VO_x samples prepared under different conditions are presented in Figure 2. Through the crystal structure analysis, the pattern of Figure 2a could be ascribed to the orthorhombic phase of $V_3O_7{\cdot}H_2O$ (PDF# 28-1433) with characteristic peaks of (020), (120), (130), etc. Two sets of diffraction peaks can be deconstructed from Figure 2b, which belongs to the orthorhombic $V_3O_7{\cdot}H_2O$ (major component) and monoclinic VO_2 (B) (minor component with asterisk mark, PDF# 31-1438) with peaks of (200), (110), (−311), etc., respectively. This indicates that the ethanol, as a weak reducing agent, would lead to the conversion of V^{5+} to V^{4+} and meanwhile be oxidized to aldehyde itself. When maintaining a relatively high ethanol content, like the sample $V_3O_7{\cdot}H_2O/VO_2$ (B)* NBs, and bringing in MWCNTs, the monoclinic VO_2 (B) was primarily acquired as shown in Figure 2c. This result shows that MWCNTs would play the role of inductive reducibility during hydrothermal treatment, which may owe to the oxygen-contained functional groups on the surface of MWCNTs generated during the mixed acid treatment and hydrothermal reaction. There is a broad peak envelope at $2\theta \approx 26°$ in Figure 2c, which was caused by the (002) plane of amorphous MWCNTs during the sample VO_2 (B) NBs/MWCNTs [16,17]. For sample V_2O_5 NBs, whose XRD pattern in Figure 2d confirms its orthorhombic V_2O_5 phase (PDF# 41-1426), with a typical crystal plane of (200), (001), (101), etc., illustrating the transformation of V^{4+} to V^{5+} when $V_3O_7{\cdot}H_2O$ was subject to sintering in air.

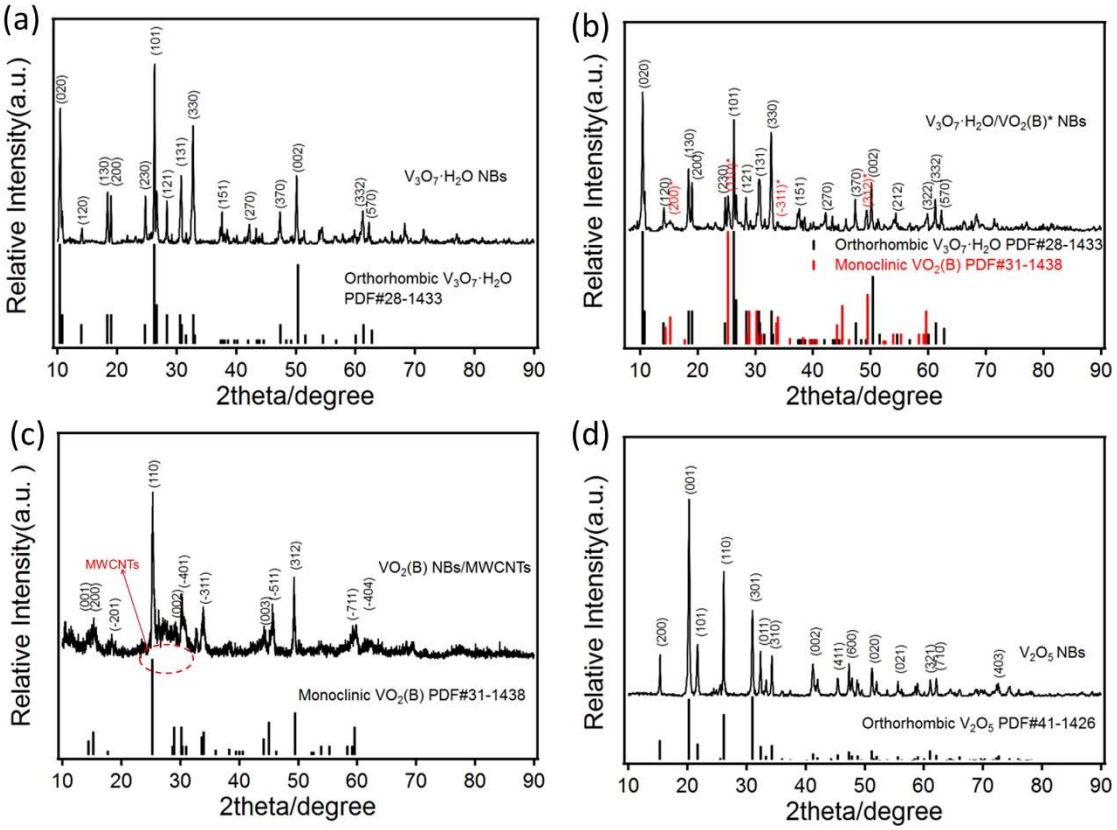

Figure 2. XRD patterns of $V_3O_7{\cdot}H_2O$ NBs (**a**), $V_3O_7{\cdot}H_2O/VO_2$ (B)* NBs (**b**), VO_2 (B) NBs/MWCNTs (**c**) and V_2O_5 NBs (**d**).

SEM images of $V_3O_7{\cdot}H_2O$ NBs (a), $V_3O_7{\cdot}H_2O/VO_2$ (B)* NBs (b), VO_2 (B) NBs/MWCNTs (c) and V_2O_5 NBs (d) are shown in Figure 3. It can be seen that all of them display one-dimensional nanobelted morphology with a width of 100–300 nm and a length of over 10 microns. Due to the role of energy modulation under hydrothermal conditions, the growth kinetics of the vanadium oxide precursor is faster in a specific direction during the process of self-assembly crystallization and, conversely, the growth in other orientations are inhibited, resulting in a one-dimensional VO_x nano-belted morphology. In Figure 3c, VO_2 (B) NBs were evenly mingled with MWCNTs. In addition, SEM images of VO_2 (B) NBs/MWCNTs (Figure 3c) and V_2O_5 NBs (Figure 3d) also demonstrate that the adding of MWCNTs or post-sintering will not change the 1D nanostructure of VO_x samples, but result in the further decrease or increase of V valence as recognized by the XRD detections.

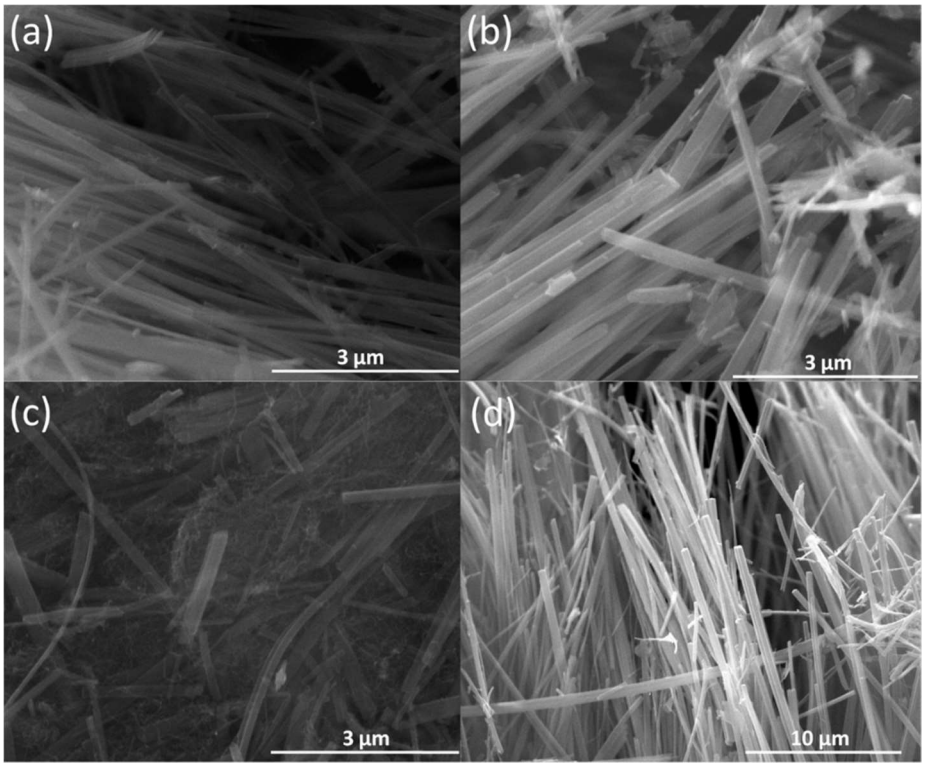

Figure 3. SEM images of $V_3O_7{\cdot}H_2O$ NBs (**a**), $V_3O_7{\cdot}H_2O/VO_2$ (B)* NBs (**b**), VO_2 (B) NBs/MWCNTs (**c**) and V_2O_5 NBs (**d**).

Figure 4 illustrates TEM and HRTEM (High-Resolution TEM) images of $V_3O_7{\cdot}H_2O$ NBs (a,b), VO_2 (B) NBs/MWCNTs (c,d) and V_2O_5 NBs (e,f). We can see from the TEM images (a,c,e) that the diameter of these samples distributes approximately between 100–300 nm, which is in accordance with previous SEM observations. Figure 4b gives the lattice fringes of (101) and (200) planes with distances of 0.338 nm and 0.466 nm for $V_3O_7{\cdot}H_2O$ NBs [18,19]. The inset shows the corresponding SAED pattern. The HRTEM image of VO_2 (B), whose (−201) crystal plane is marked with the space of ~0.5 nm, is presented in Figure 4d. Figure 4f demonstrates the (110) crystal plane for V_2O_5 NBs with a distance of 0.341 nm, as well as its SAED pattern in the upper right corner [20,21]. Thus, it could be learned that the results of TEM characterizations are consistent with those values from the calculations of the associated XRD peak positions based on the Scherrer formula.

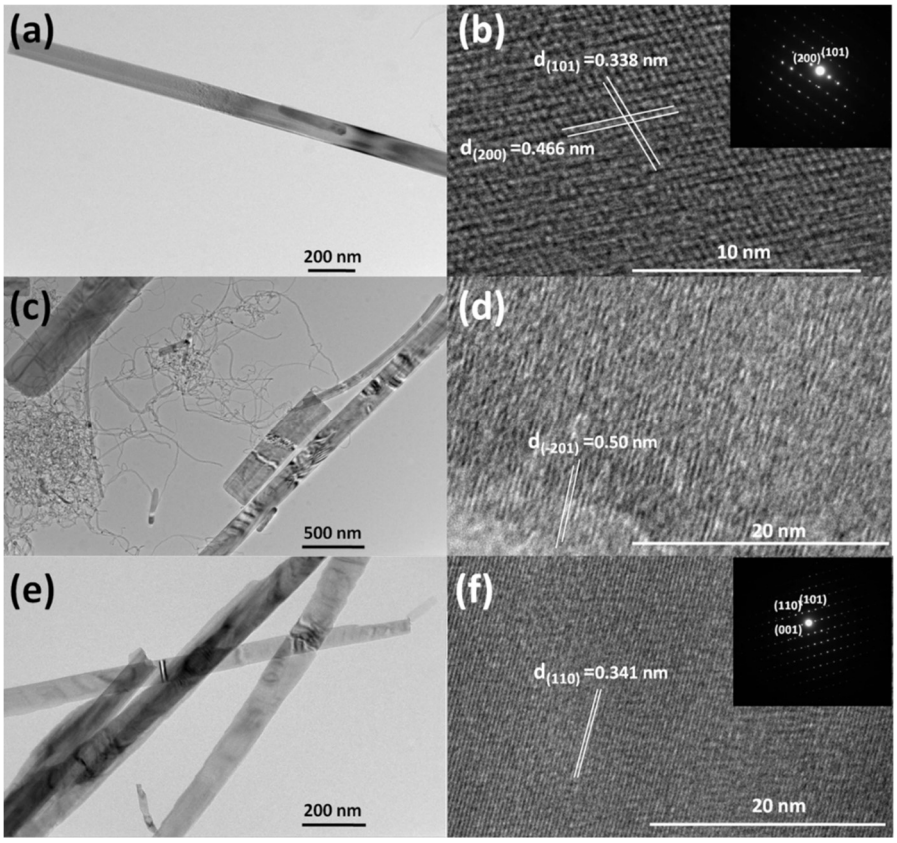

Figure 4. TEM and HRTEM images of $V_3O_7{\cdot}H_2O$ NBs (**a**,**b**), VO_2 (B) NBs/MWCNTs (**c**,**d**) and V_2O_5 NBs (**e**,**f**); the insets in (**b**) and (**f**) show SAED patterns.

FTIR spectra of the as-prepared four samples are shown in Figure 5. The characteristic absorption peaks near 1000 cm^{-1} (976, 980, 1007, 1016, 1020 and 1022 cm^{-1}) can be attributed to stretching vibrations of terminal oxygen bonds (V=O). It should be noted that the appearance of relatively low wave numbers (976, 980 and 1007 cm^{-1}) for V=O vibrations is caused by the V^{4+} in $V_3O_7{\cdot}H_2O$ NBs, $V_3O_7{\cdot}H_2O/VO_2$ (B)* NBs and VO_2 (B) NBs/MWCNTs because the bond length of V^{4+}=O is longer than that of V^{5+}=O, leading to the decrease of frequency [22]. The peaks at 802 cm^{-1} and below 600 cm^{-1} (449, 480, 546, 557, 567 and 577 cm^{-1}) emerge because of the vibration modes of the doubly coordinated oxygen (V-O-V) bonds in V_2O_5 and the triply coordinated oxygen (V_3–O) bonds within VO_x, respectively [23]. The slight shifting for these V–O coordinated vibration peaks among different samples may be connected with the microscopic stress change in the crystal lattice. Besides, the absorption peaks at 1628–1633 cm^{-1} and 3412–3444 cm^{-1} could be ascribed to the bending and stretching vibrations of H–O bonds from the absorbed/bound water in samples, respectively [24,25]. The wave-number at ~2350 cm^{-1} is due to the contamination of CO_2 molecules in the measuring atmosphere [26].

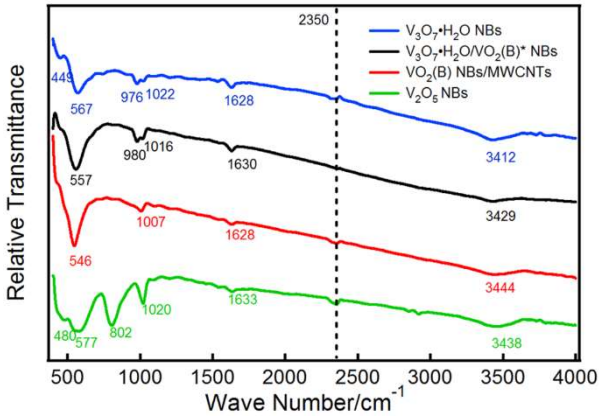

Figure 5. FTIR spectra of V_3O_7·H_2O NBs, V_3O_7·H_2O/VO_2 (B)* NBs, VO_2 (B) NBs/MWCNTs and V_2O_5 NBs between 400–4000 cm^{-1}.

The initial three CV curves of the four samples between 1.5–4 V are depicted in Figure 6.

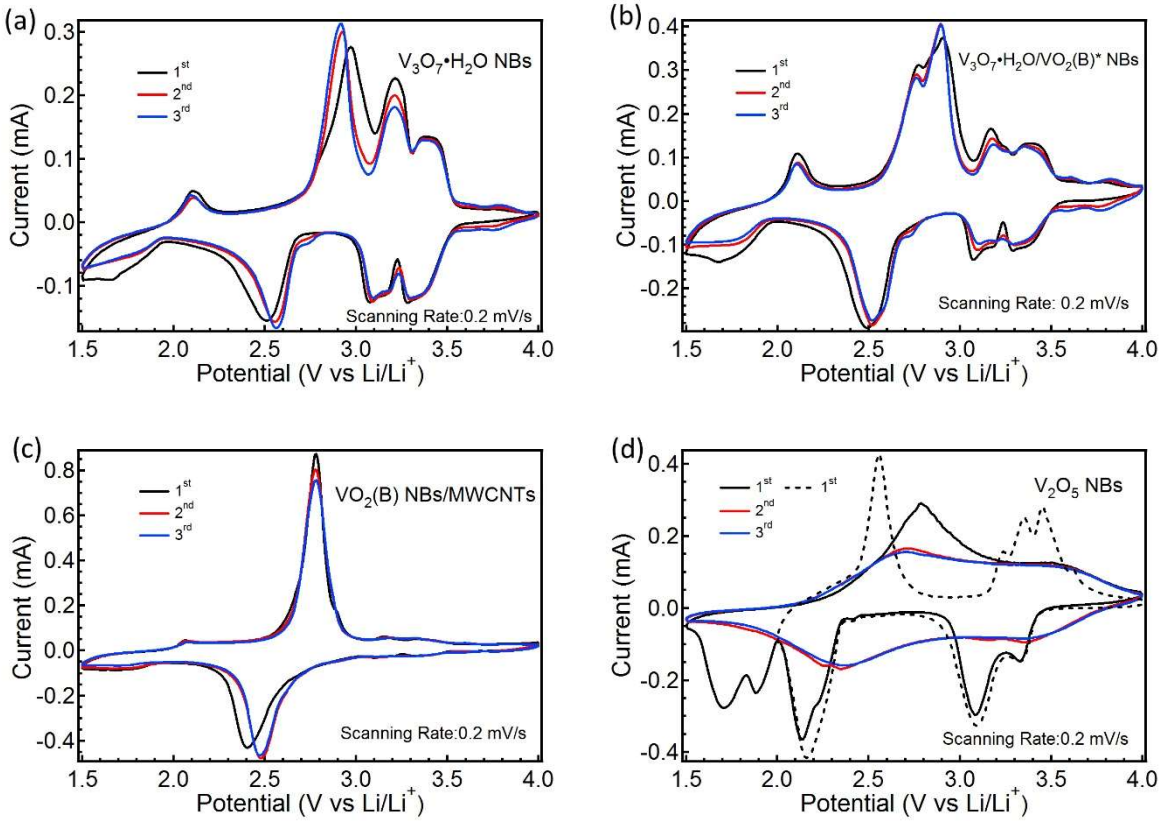

Figure 6. CV curves of V_3O_7·H_2O NBs (**a**), V_3O_7·H_2O/VO_2 (B)* NBs (**b**), VO_2 (B) NBs/MWCNTs (**c**) and V_2O_5 NBs (**d**) with a scanning speed of 0.2 mV s^{-1}.

For V_3O_7·H_2O NBs, four pairs of stable cathodic/anodic peaks appear at ~3.30/3.37, 3.09/3.21, 2.56/2.92 and 1.80/2.11 V, in which two pairs of redox peaks at ~3.30/3.37 and 3.09/3.21 V between 3.0–3.5 V correspond to the reaction:

$$V_3O_7{\cdot}H_2O + Li^+ + e^- \leftrightarrow LiV_3O_7{\cdot}H_2O. \quad (1)$$

The other pair of peaks at ~2.56/2.92 V between 2.3–3.0 V can be ascribable to the reaction:

$$LiV_3O_7{\cdot}H_2O + Li^+ + e^- \leftrightarrow Li_2V_3O_7{\cdot}H_2O. \quad (2)$$

Another pair of peaks at ~1.80/2.11 V in the region of 1.5–2.3 V is related with the reaction:

$$Li_2V_3O_7{\cdot}H_2O + xLi^+ + xe^- \leftrightarrow Li_{2+x}V_3O_7{\cdot}H_2O\ (x < 1). \quad (3)$$

Both Equations (1) and (2) involve the conversion of $V^{5+}\leftrightarrow V^{4+}$, whereas Equation (3) refers to the partial $V^{4+}\leftrightarrow V^{3+}$ [27,28]. The CV curves of VO_2 (B) NBs/MWCNTs are shown in Figure 6c. One pair of predominant redox peaks emerges at ~2.48/2.78 V, which is the typical trait for the monoclinic VO_2 (B) phase during the repeated Li^+ insertion/extraction, corresponding to the reaction [29]:

$$VO_2\ (B) + xLi^+ + xe^- \leftrightarrow Li_xVO_2\ (B)\ (x \approx 0.5) \quad (4)$$

According to the analysis of a previous XRD, we know that $V_3O_7{\cdot}H_2O/VO_2$ (B)* NBs contain a small quantity of the VO_2 (B) phase. Thus, the overall outline of the CV curves for $V_3O_7{\cdot}H_2O/VO_2$ (B)* NBs in Figure 6b is similar to that of the $V_3O_7{\cdot}H_2O$ NBs, but there is an upward anodic shoulder peak appearing at ~2.76 V and a slightly lower shift for the downward cathodic peak from 2.56 to 2.52 V. Further, the relative peak area between 2.3–3.0 V for $V_3O_7{\cdot}H_2O/VO_2$ (B)* NBs is larger compared to the $V_3O_7{\cdot}H_2O$ NBs. These changes are concerned with the redox process of $V^{4+}\leftrightarrow V^{3+}$ in the VO_2 (B) phase contained. The solid and dotted lines in Figure 6d present the CV curves of the V_2O_5 NBs at the voltage sweep range of 1.5–4 V and 2–4 V, respectively. During the initial Li^+ intercalation between 1.5–4 V, the cathodic peaks at ~3.33, 3.08 and 2.14 V correspond to the phase transitions of α-$Li_xV_2O_5$ to ε-$Li_xV_2O_5$, ε-$Li_xV_2O_5$ to δ-$Li_xV_2O_5$ ($x < 1$) and δ-$Li_xV_2O_5$ to γ-$Li_xV_2O_5$ ($1 < x < 2$), respectively. When the working voltage lowers below 2 V, the irreversible phase transition happens from γ-$Li_xV_2O_5$ to ω-$Li_xV_2O_5$($x > 2$) [30,31]. Therefore, the anodic peaks associated with the phase transitions above do not arise in the subsequent Li^+ extraction process. There is only a wide anodic peak at ~2.71 during the following 2nd–3rd cycles, illustrating the amorphous features and irreversible structural change of V_2O_5 NBs operating in this voltage region (1.5–4 V). When V_2O_5 NBs work at 2–4 V, three pairs of primary redox peaks appear at ~3.33/3.45, 3.08/3.35 and 2.14/2.56 V, indicating the reversible phase transition between α-$Li_xV_2O_5 \leftrightarrow \gamma$-$Li_xV_2O_5$ ($x < 2$) [31,32]. Thus, the subsequent GCD evaluation for V_2O_5 NBs was performed between 2–4 V.

GCD profiles of four samples are plotted in Figure 7 at the 1st, 2nd, 5th, 20th and 50th charge/discharge cycles under 100 mA/g. Because VO_x NBs non-embedded by Li^+ are at a full charge state in the beginning, there is only the 1st discharge process for all samples. With regard to the $V_3O_7{\cdot}H_2O$ NBs in Figure 7a, four voltage plateaus emerged in sequence at ~3.3, 3.1, 2.6 and 1.8 V during the discharge (Li^+ intercalation), which are related with the four downward cathodic peaks in its CV curve. Conversely, the voltage plateaus turn up at ~2.1, 2.8, 3.2 and 3.4 V sequentially during the charge (Li^+ de-intercalation), corresponding to its upward anodic peaks in the CV. For the VO_2 (B) NBs/MWCNTs in Figure 7c, there was an obvious discharge and charge plateau at 2.5 V and 2.6 V, respectively, which are concerned with the pair of dominant redox peaks in its CV. The GCD profile of the $V_3O_7{\cdot}H_2O/VO_2$ (B)* NBs in Figure 7b is similar to that of $V_3O_7{\cdot}H_2O$ NBs. However, the discharge plateau at ~2.5 V was elongated visibly. Further, the charge plateau at ~2.8 V was also lengthened and split into two close plateaus. These variations in GCD for the $V_3O_7{\cdot}H_2O/VO_2$ (B)* NBs are consistent with the changes in its CV curves. As for the V_2O_5 NBs in Figure 7, when working between 2–4 V, the stable GCD profile was formed through the first few discharge/charge activations, whose reversible plateaus correspond to the prime redox peaks in its CV (dotted line). From the standpoint of median discharge voltage (MDV), $V_3O_7{\cdot}H_2O$ NBs, VO_2 (B) NBs/MWCNTs and V_2O_5 NBs show the MDV values of ~2.61–2.70 V, ~2.50 V and ~2.68–2.71 V during their operating voltage ranges, respectively.

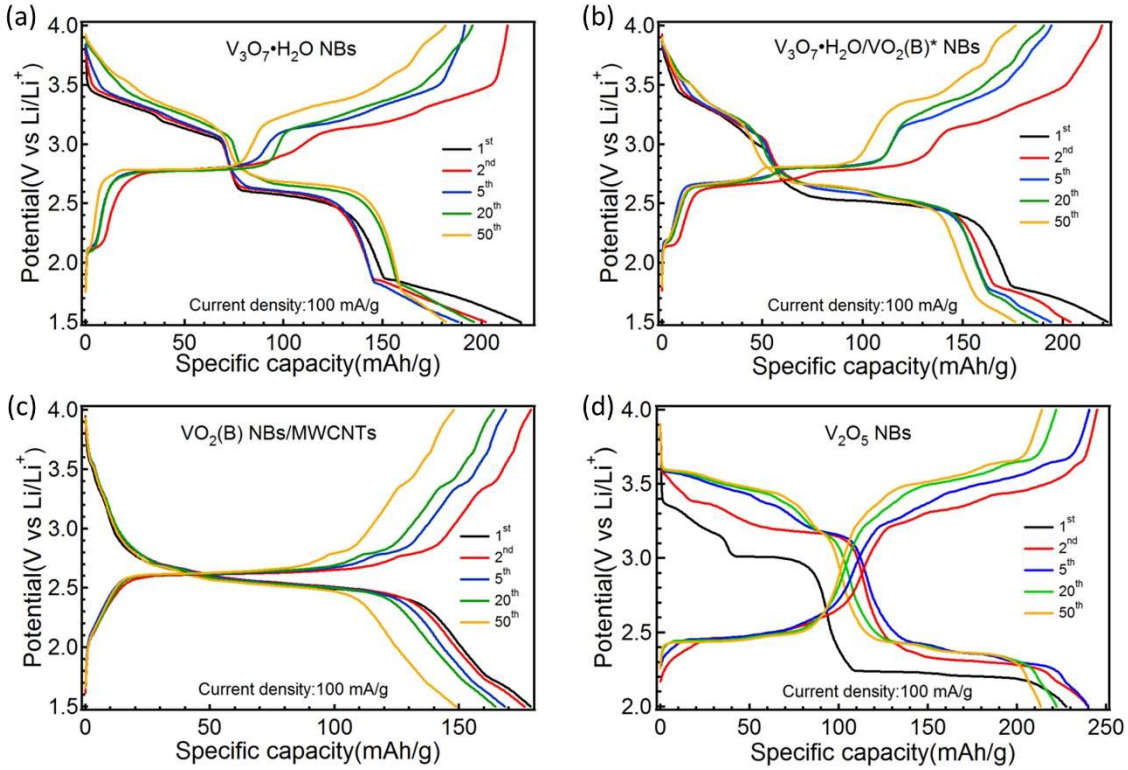

Figure 7. Galvanostatic charge/discharge profiles of $V_3O_7{\cdot}H_2O$ NBs (**a**), $V_3O_7{\cdot}H_2O/VO_2$ (B)* NBs (**b**), VO_2 (B) NBs/MWCNTs (**c**) and V_2O_5 NBs (**d**) under different cycles at the current density of 100 mA g^{-1}.

The cycling performances of the four samples at 100 mA/g are successively displayed in Figure 8a–d. $V_3O_7{\cdot}H_2O$ NBs in Figure 8a delivered a highest specific capacity of 219.8 mAh/g at the first discharge and kept at 181.9 mAh/g after 50 cycles. As shown in Figure 8b, $V_3O_7{\cdot}H_2O/VO_2$ (B)* NBs presented the highest discharge capacity of 222.2 mAh/g for the first cycle and remained at 176.2 mAh/g on the 50th discharge. The VO_2 (B) NBs/MWCNTs in Figure 8c gave the largest value of 178.8 mAh/g at the first discharge and maintained at 148.9 mAh/g for the 50th cycle. Although the specific capacity of VO_2 (B) NBs is unsatisfactory, its charge/discharge plateau is very flat. During practical usage, VO_2 (B) NBs will output stable voltage and power. The highest capacity of 240.4 mAh/g was released at the third discharge for V_2O_5 NBs after initial two activation cycles in Figure 8d. When the cycling number went to the 50th cycle, this value remained at 213.3 mAh/g. We can see from the above cycling diagrams that the capacities for all samples exhibit periodic fluctuation with cyclic numbers, which are due to the large diurnal temperature variation between 10–21 °C in the local lab. This result shows that temperature has a non-negligible effect on the Li^+ storage property for all VO_x samples. It is noteworthy that V_2O_5 NBs possesses higher capacity and cycling stability owing to their complete V^{5+} and better crystallinity. Thus, the rate capability of V_2O_5 NBs was further evaluated, as illustrated in Figure 8e. The typical CD curves at the last cycle under different current densities of 50, 100, 200, 400 and back to 50 mA/g are shown in Figure 8f, whose corresponding discharge capacities were 237.1, 217.1, 199.9, 184.9 and 221.8 mAh/g, respectively.

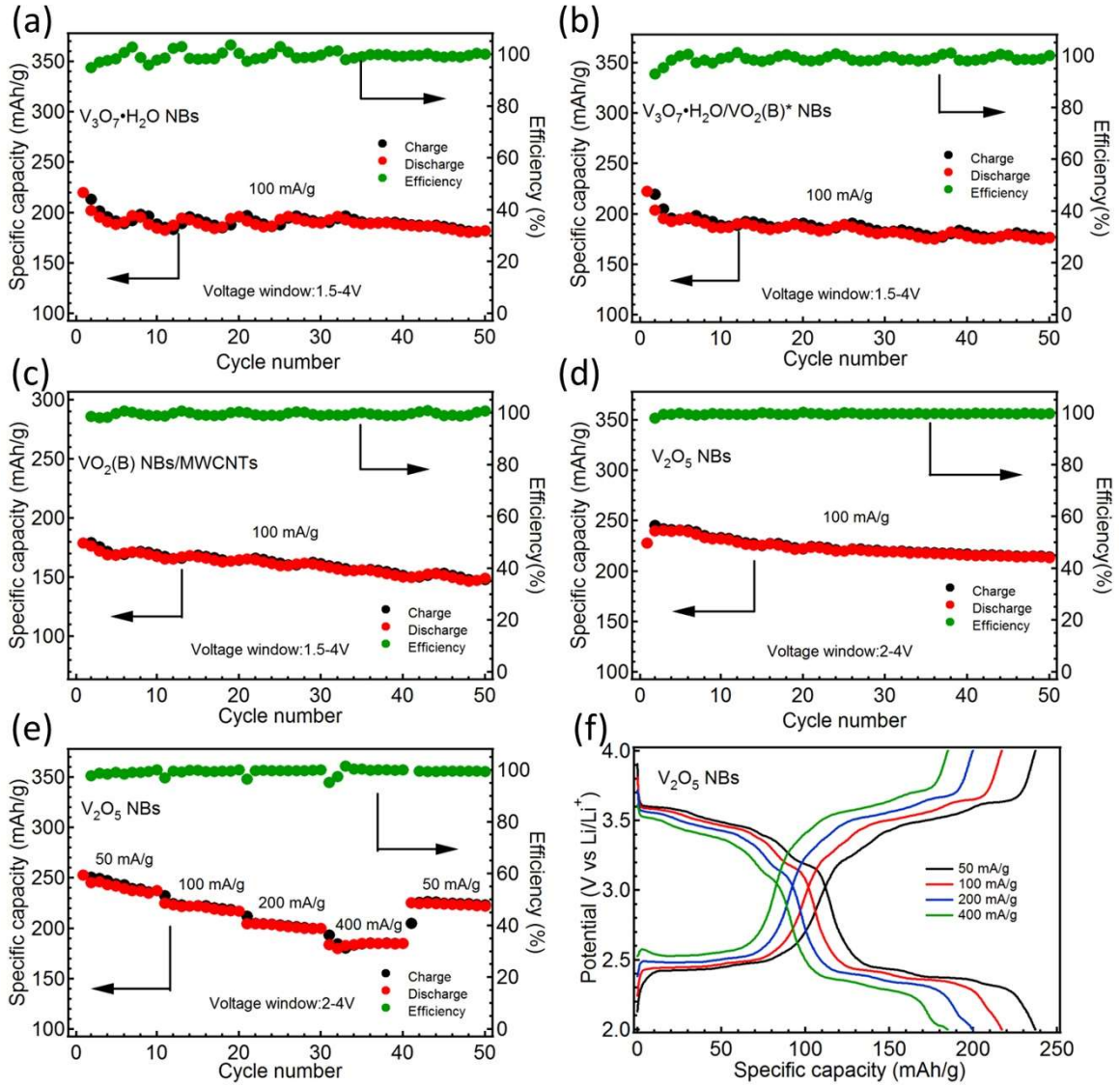

Figure 8. Cycling performances and coulombic efficiencies of $V_3O_7{\cdot}H_2O$ NBs (**a**), $V_3O_7{\cdot}H_2O/VO_2$ (B)* NBs (**b**), VO_2 (B) NBs/MWCNTs (**c**) and V_2O_5 NBs (**d**) at 100 mA g^{-1}; rate capability (**e**) and typical galvanostatic charge/discharge (GCD) profiles (**f**) of V_2O_5 NBs under varying current densities.

Nyquist plots and Warburg coefficients (A_w) linear fittings of four samples at the SOC of ~3 V are illustrated in Figure 9a,b, respectively. Nyquist plots are composed of a compressed semicircle arc at a high-frequency region and an oblique straight line at low-frequency region, in which the X-axis intercept of semicircle on the extreme left denotes the equivalent series resistance (R_e), the span of the semicircle is associated with the charge transfer resistance (R_{ct}) at the electrolyte/electrode interface and the sloping line is connected with the Li^+ diffusion in the solid electrode [33]. Based on the equivalent circuit (in which CPE is the constant-phase element, Wo represents the Warburg impedance) in the inset of Figure 9a, we can get the fitted values of R_e and R_{ct} for four samples, as listed in Table 1. All of their R_e values are small and distribute at 4–6 Ω. The R_{ct} of VO_2 (B) NBs/MWCNTs is the lowest, which could be due to incorporation of conducting MWCNTs as well as the existence of predominant V^{4+} in the sample [34,35]. The lower R_{ct} is beneficial to the migration and transport of Li^+ at the electrolyte/electrode interface.

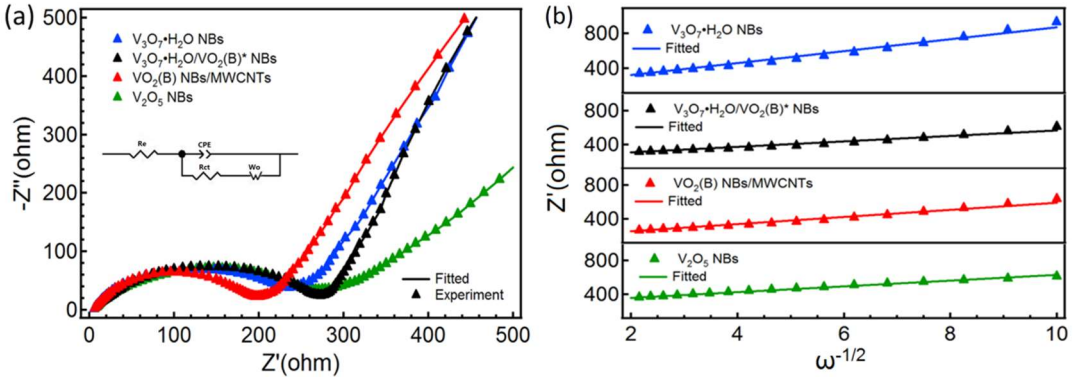

Figure 9. Nyquist plots (**a**) and dependences (**b**) of real resistance (Z′) on reciprocal of square root of angular frequency (ω) for all samples; the inset in (**a**) illustrating the equivalent circuit.

Table 1. Fitted values of R_e, R_{ct} and A_w for all prepared samples.

Samples	R_e (Ω)	R_{ct} (Ω)	A_w ($\Omega \cdot s^{-1/2}$)
$V_3O_7 \cdot H_2O$ NBs	5.1	210.5	69.0
$V_3O_7 \cdot H_2O/VO_2$(B)* NBs	4.6	276.9	33.1
VO_2(B) NBs/MWCNTs	5.1	199.8	42.9
V_2O_5 NBs	5.7	230.1	34.4

To discuss the diffusion of Li^+ during the active VO_x NBs, we need to access the Li^+ diffusion coefficient (D_{Li+}) of the samples, which can be expressed as [36]:

$$D_{Li^+} = \frac{R^2T^2}{2n^4F^4A^2C^2{A_w}^2} \quad (5)$$

where, R (ideal gas constant), T (absolute temperature), n (electron transfer number per mole), F (Faraday's constant), A (geometric area of electrode) and C (molar concentration of Li^+) are fixed experimental parameters under certain sample and test condition. A_w is the Warburg coefficient that is related to the Li^+ diffusion process. Because $D_{Li+} \propto {A_w}^{-2}$, we can use the value of A_w to quantitatively evaluate the Li^+ diffusion. According to the equation $Z' = R_e + R_{ct} + A_w\omega^{-1/2}$ (6) at the low-frequency region, a linear relationship between Z′ and $\omega^{-1/2}$ can be observed for all samples, as shown in Figure 9b. The slope of a straight line is the value of A_w as listed in Table 1, which would be acquired by linear fitting. The results show that $V_3O_7 \cdot H_2O/VO_2$ (B)* NBs and V_2O_5 NBs exhibit a relatively lower A_w at the given SOC, signifying the preferable diffusion behavior.

4. Conclusions

In this work, three kinds of 1D VO_x NBs, referring to $V_3O_7 \cdot H_2O$ NBs, VO_2 (B) NBs and V_2O_5 NBs, which have different crystalline structure and vanadium valence, were synthesized under hydrothermal conditions merely by adjusting and adding the reductive ingredients (ethanol and MWCNTs), as well as conducting post-sintering treatment. XRD and SEM demonstrated the crystal structures and morphologies of acquired VO_x NBs (showing a typical width of 100–300 nm and over 10 microns in length). TEM and FTIR revealed their micro-architectures and components. The electrochemical Li^+ storage properties of these VO_x NBs were systematically analyzed and compared with each other as cathode materials for LIBs. Among them, V_2O_5 NBs exhibited a relatively larger capacity, higher median discharge voltage and more stable cycling performance, which can be attributed to its higher V valence state and better crystallization. From the perspective of actual use, although VO_2 (B) NBs showed an unsatisfactory specific capacity (148.9 mAh/g after 50 cycles at 100 mA/g), it displayed just one flat discharge platform at the testing potential window, which benefits the stable output of working voltage and power in practical battery applications. These representative 1D VO_x NBs derived from a

simple hydrothermal reaction could be used as promising cathode candidates for future LIBs according to actual demands.

Supplementary Materials: The following are available online at http://www.mdpi.com/2079-4991/9/4/624/s1, Figure S1. SEM images of commercial V_2O_5 powder at 1000 (a) and 5000 (b) times magnification, respectively.

Author Contributions: Y.J. and X.Z. carried out the experiments and wrote the manuscript together. X.Z. conceived the experimental procedure. X.C. and J.W. provided useful help in electrochemical tests. L.G. and M.S. gave necessary assistance for the characterization of samples. Y.R. and Z.L. put forward valuable advices for the improvement of article.

Funding: This research was funded by the National Natural Science Foundation of China (Grant Nos. 61664009, 51771169), Young/Middle-aged Backbone Teacher Cultivating Scheme of Yunnan University (Grant No. C176220200) and High-end Scientific & Technological Talents Introduction Project of Yunnan Province (Grant No. 2013HA019).

Conflicts of Interest: The authors declare no conflict of interest.

References

1. Manthiram, A. An Outlook on Lithium Ion Battery Technology. *ACS Cent. Sci.* **2017**, *3*, 1063–1069. [CrossRef] [PubMed]
2. Wang, Y.; Cao, G. Synthesis and Enhanced Intercalation Properties of Nanostructured Vanadium Oxides. *Cheminform* **2006**, *37*, 2787–2804.
3. McNulty, D.; Buckley, D.N.; O'Dwyer, C. Synthesis and electrochemical properties of vanadium oxide materials and structures as Li-ion battery positive electrodes. *J. Power Sources* **2014**, *267*, 831–873. [CrossRef]
4. Liu, X.; Zeng, J.; Yang, H.; Zhou, K.; Pan, D. V_2O_5-Based nanomaterials: Synthesis and their applications. *RSC Adv.* **2018**, *8*, 4014–4031. [CrossRef]
5. Liu, Y.; Wang, Y.; Zhang, Y.; Liang, S.; Pan, A. Controllable Preparation of V_2O_5/Graphene Nanocomposites as Cathode Materials for Lithium-Ion Batteries. *Nanoscale Res. Lett.* **2016**, *11*, 549. [CrossRef]
6. Armer, C.F.; Yeoh, J.S.; Li, X.; Lowe, A. Electrospun vanadium-based oxides as electrode materials. *J. Power Sources* **2018**, *395*, 414–429. [CrossRef]
7. Armstrong, M.J.; Burke, D.M.; Gabriel, T.; O'Regan, C.; O'Dwyer, C.; Petkov, N.; Holmes, J.D. Carbon nanocage supported synthesis of V_2O_5 nanorods and V_2O_5/TiO_2 nanocomposites for Li-ion batteries. *J. Mater. Chem. A* **2013**, *1*, 12568. [CrossRef]
8. Liu, M.; Su, B.; Tang, Y.; Jiang, X.; Yu, A. Recent Advances in Nanostructured Vanadium Oxides and Composites for Energy Conversion. *Adv. Energy Mater.* **2017**, *7*, 1700885. [CrossRef]
9. Petnikota, S.; Chua, R.; Zhou, Y.; Edison, E.; Srinivasan, M. Amorphous Vanadium Oxide Thin Films as Stable Performing Cathodes of Lithium and Sodium-Ion Batteries. *Nanoscale Res. Lett.* **2018**, *13*, 363. [CrossRef]
10. Li, S.; Liu, G.; Liu, J.; Lu, Y.; Yang, Q.; Yang, L.Y.; Yang, H.R.; Liu, S.; Lei, M.; Han, M. Carbon fiber cloth@VO_2 (B): Excellent binder-free flexible electrodes with ultrahigh mass-loading. *J. Mater. Chem. A* **2016**, *4*, 6426–6432. [CrossRef]
11. Li, Z.; Sun, H.; Xu, J.; Zhu, Q.; Chen, W.; Zakharova, G.S. The synthesis, characterization and electrochemical properties of $V_3O_7{\cdot}H_2O$/CNT Nanocomposite. *Solid State Ion.* **2014**, *262*, 30–34. [CrossRef]
12. Niu, C.; Li, J.; Jin, H.; Shi, H.; Zhu, Y.; Wang, W.; Cao, M. Self-template processed hierarchical V_2O_5 nanobelts as cathode for high performance lithium ion battery. *Electrochim. Acta* **2015**, *182*, 621–628. [CrossRef]
13. Rui, X.; Sim, D.; Xu, C.; Liu, W.; Tan, H.; Wong, K.; Hng, H.H.; Lim, T.M.; Yan, Q. One-pot synthesis of carbon-coated VO_2(B) nanobelts for high-rate lithium storage. *RSC Adv.* **2012**, *2*, 1174–1180. [CrossRef]
14. Yu, Y.; Li, J.; Wang, X.; Chang, B.; Wang, J.; Ahmad, M.; Sun, H. Oxygen vacancies enhance lithium storage performance in ultralong vanadium pentoxide nanobelt cathodes. *J. Colloid Interface Sci.* **2018**, *539*, 118–125. [CrossRef]
15. Zhang, C.; Song, H.; Zhang, C.; Liu, C.; Liu, Y.; Cao, G. Interface Reduction Synthesis of $H_2V_3O_8$ Nanobelts–Graphene for High-Rate Li-Ion Batteries. *J. Phys. Chem. C* **2015**, *119*, 11391–11399. [CrossRef]
16. Baro, M.; Nayak, P.; Baby, T.T.; Ramaprabhu, S. Green approach for the large-scale synthesis of metal/metal oxidenanoparticle decorated multiwalled carbon nanotubes. *J. Mater. Chem. A* **2013**, *1*, 482–486. [CrossRef]
17. Wei, S.; Wang, X.; Zhang, R.; Hu, H.; Shen, Y.; Liu, J. Preparation and performance of spherical $FeF_{2.5}{\cdot}0.5H_2O$ nanoparticles wrapped by MWCNTs as cathode material of lithium ion batteries. *RSC Adv.* **2016**, *6*, 97759–97769. [CrossRef]

18. Li, H.; Zhai, T.; He, P.; Wang, Y.; Hosono, E.; Zhou, H. Single-crystal $H_2V_3O_8$ nanowires: A competitive anode with large capacity for aqueous lithium-ion batteries. *J. Mater. Chem.* **2011**, *21*, 1780–1787. [CrossRef]
19. Wang, D.; Wei, Q.; Sheng, J.; Hu, P.; Yan, M.; Sun, R.; Xu, X.; An, Q.; Mai, L. Flexible additive free $H_2V_3O_8$ nanowire membrane as cathode for sodium ion batteries. *Phys. Chem. Chem. Phys.* **2016**, *18*, 12074–12079. [CrossRef]
20. An, Q.; Zhang, P.; Wei, Q.; He, L.; Xiong, F.; Sheng, J.; Wang, Q.; Mai, L. Top-down fabrication of three-dimensional porous V_2O_5 hierarchical microplates with tunable porosity for improved lithium battery performance. *J. Mater. Chem. A* **2014**, *2*, 3297–3302. [CrossRef]
21. Li, W.D.; Xu, C.Y.; Pan, X.L.; Huang, Y.D.; Zhen, L. High capacity and enhanced structural reversibility of β-$Li_xV_2O_5$ nanorods as the lithium battery cathode. *J. Mater. Chem. A* **2013**, *1*, 5361. [CrossRef]
22. Ahirrao, D.J.; Mohanapriya, K.; Jha, N. V_2O_5 nanowires-graphene composite as an outstanding electrode material for high electrochemical performance and long-cycle-life supercapacitor. *Mater. Res. Bull.* **2018**, *108*, 73–82. [CrossRef]
23. Laorodphan, N.; Pooddee, P.; Kidkhunthod, P.; Kunthadee, P.; Tapala, W.; Puntharod, R. Boron and pentavalent vanadium local environments in binary vanadium borate glasses. *J. Non-Cryst. Solids* **2016**, *453*, 118–124. [CrossRef]
24. Hassan, N.; Riaz, J.; Qureshi, M.T.; Razaq, A.; Rahim, M.; Toufiq, A.M.; Shakoor, A. Vanadium oxide (V_2O_3) for energy storage applications through hydrothermal route. *J. Mater. Sci. Mater. Electron.* **2018**, *29*, 16021–16026. [CrossRef]
25. Roppolo, M.; Jacobs, C.B.; Upreti, S.; Chernova, N.A.; Whittingham, M.S. Synthesis and characterization of layered and scrolled amine-templated vanadium oxides. *J. Mater. Sci.* **2008**, *43*, 4742–4748. [CrossRef]
26. Bordelet, G.; Yamaguchi, I.; Manabe, T.; Tsuchiya, T. Low temperature vanadium oxide thin film sintering by thermal and excimer-laser-assisted Metal-Organic Deposition (MOD). *Ceram. Int.* **2018**, *44*, S26–S29. [CrossRef]
27. An, Q.; Sheng, J.; Xu, X.; Wei, Q.; Zhu, Y.; Han, C.; Niu, C.; Mai, L. Ultralong $H_2V_3O_8$ nanowire bundles as a promising cathode for lithium batteries. *New J. Chem.* **2014**, *38*, 2075–2080. [CrossRef]
28. Liu, P.; Bian, K.; Zhu, K.; Xu, Y.; Gao, Y.; Luo, H.; Lu, L.; Wang, J.; Liu, J.; Tai, G. Ultrathin Nanoribbons of in Situ Carbon-Coated $V_3O_7{\cdot}H_2O$ for High-Energy and Long-Life Li-Ion Batteries: Synthesis, Electrochemical Performance, and Charge-Discharge Behavior. *ACS Appl. Mater Interfaces* **2017**, *9*, 17002–17012. [CrossRef]
29. Mai, L.; Wei, Q.; An, Q.; Tian, X.; Zhao, Y.; Xu, X.; Xu, L.; Chang, L.; Zhang, Q. Nanoscroll buffered hybrid nanostructural VO_2 (B) cathodes for high-rate and long-life lithium storage. *Adv. Mater.* **2013**, *25*, 2969–2973. [CrossRef]
30. Shao, L.; Wu, K.; Lin, X.; Shui, M.; Ma, R.; Wang, D.; Long, N.; Ren, Y.; Shu, J. Sol–gel preparation of V_2O_5 sheets and their lithium storage behaviors studied by electrochemical and in-situ X-ray diffraction techniques. *Ceram. Int.* **2014**, *40*, 6115–6125. [CrossRef]
31. Sakunthala, A.; Reddy, M.V.; Selvasekarapandian, S.; Chowdari, B.V.R.; Selvin, P.C. Energy storage studies of bare and doped vanadium pentoxide, $(V_{1.95}M_{0.05})O_5$, M = Nb, Ta, for lithium ion batteries. *Energy Environ. Sci.* **2011**, *4*, 1712. [CrossRef]
32. Xu, Y.; Dunwell, M.; Fei, L.; Fu, E.; Lin, Q.; Patterson, B.; Yuan, B.; Deng, S.; Andersen, P.; Luo, H.; et al. Two-dimensional V_2O_5 sheet network as electrode for lithium-ion batteries. *ACS Appl. Mater. Interfaces* **2014**, *6*, 20408–20413. [CrossRef]
33. Tang, K.; Yu, X.; Sun, J.; Li, H.; Huang, X. Kinetic analysis on $LiFePO_4$ thin films by CV, GITT, and EIS. *Electrochim. Acta* **2011**, *56*, 4869–4875. [CrossRef]
34. Jiang, H.; Wei, Z.; Cai, X.; Lai, L.; Ma, J.; Huang, W. A cathode for Li-ion batteries made of vanadium oxide on vertically aligned carbon nanotube arrays/graphene foam. *Chem. Eng. J.* **2019**, *359*, 1668–1676. [CrossRef]
35. Liu, D.; Liu, Y.; Garcia, B.B.; Zhang, Q.; Pan, A.; Jeong, Y.H.; Cao, G. V_2O_5 xerogel electrodes with much enhanced lithium-ion intercalation properties with N_2 annealing. *J. Mater. Chem.* **2009**, *19*, 8789. [CrossRef]
36. Song, H.; Luo, M.; Wang, A. High Rate and Stable Li-Ion Insertion in Oxygen-Deficient LiV_3O_8 Nanosheets as a Cathode Material for Lithium-Ion Battery. *ACS Appl. Mater. Interfaces* **2017**, *9*, 2875–2882. [CrossRef]